JOURNAL OF GEOPHYSICAL RESEARCH: PLANETS, VOL. 118, 1–13, doi:10.1002/jgre.20090, 2013

Model-based constraints on the lunar exosphere derived from ARTEMIS pickup ion observations in the terrestrial magnetotail

A. R. Poppe,[1,2] J. S. Halekas,[1,2] R. Samad,[1] M. Sarantos,[2,3,4] and G. T. Delory[1,2]

Received 12 February 2013; revised 30 April 2013; accepted 1 May 2013.

[1] We use Acceleration, Reconnection, Turbulence and Electrodynamics of the Moon's Interaction with the Sun (ARTEMIS) measurements of lunar exospheric pickup ions in the terrestrial magnetotail lobes combined with a particle-tracing model to constrain the source species and distributions of the lunar neutral exosphere. These pickup ions, generated by photoionization of neutral species while the Moon is in the magnetotail lobes, undergo acceleration from both the magnetotail convection electric field and the lunar surface photoelectric field, giving rise to distinct pickup ion flux, pitch angle, and energy distributions. By simulating the behavior of lunar pickup ions in the magnetotail lobes and the response of the twin ARTEMIS probes under various ambient conditions, we can constrain several physical quantities associated with these observations, including the source ion production rate and the magnetotail convection velocity (and hence, electric field). Using the model-derived source ion production rate and established photoionization rates, we present upper limits on the density of several species potentially in the lunar exosphere. In certain cases, these limits are lower than those previously reported. We also present evidence that the lunar exosphere is displaced toward the lunar dawnside while in the terrestrial magnetotail based on fits to the observed pickup ion distributions.

Citation: Poppe, A. R., J. S. Halekas, R. Samad, M. Sarantos, and G. T. Delory (2013), Model-based constraints on the lunar exosphere derived from ARTEMIS pickup ion observations in the terrestrial magnetotail, *J. Geophys. Res. Planets*, *118*, doi:10.1002/jgre.20090.

1. Introduction

[2] Despite decades of measurement, a complete census of the various constituents of the lunar neutral exosphere and a full understanding of the dynamics thereof are not yet complete. Apollo-era observations either positively detected or suggested the presence of several neutral species, including He, Ne, N_2, CH_4, CO, CO_2, Ar, and Rn, via either surface-based mass spectrometry [*Hoffman et al.*, 1973; *Hoffman and Hodges*, 1975] or the detection of energetic alpha particles from radioactive decay [*Gorenstein et al.*, 1973]. Later, optical observations of the Moon added Na and K to this list via the observation of their characteristic solar scattering emissions [*Mendillo et al.*, 1993; *Potter et al.*, 2000; *Wilson et al.*, 2006]. More recent measurements have included observations of He variability by the Lunar Reconnaissance Orbiter/Lyman Alpha Mapping Project instrument [*Stern et al.*, 2012; *Feldman et al.*, 2012] and multiple species via observations of photoionized pickup ions [*Tanaka et al.*, 2009; *Yokota et al.*, 2009; *Halekas et al.*, 2012, 2013]. Many additional species suspected of existing in the lunar exosphere have eluded direct detection, and both ground- and space-based spectroscopy have provided only upper limits on densities (cf. *Stern* [1999], Table 1).

[3] Observations of pickup ions are a powerful tool in determining the structure and dynamics of neutral exospheres at airless bodies [*Yokota and Saito*, 2005; *Hartle and Killen*, 2006]. Pickup ions originate from their parent bodies through a combination of processes, including photoionization of neutrals in planetary exospheres, sputtering of planetary surfaces by high-energy incident charged particles and/or micrometeoroids, charge-exchange, and photon- and electron-stimulated desorption. At the Moon, a combination of all of these processes exists with each method producing different fluxes and distributions of pickup ions depending on the ambient environment, although photoionization is expected to be the dominant loss mechanism [*Stern*, 1999; *Sarantos et al.*, 2012a]. Previous observations of lunar pickup ions have been reported in the solar wind and in the terrestrial magnetotail lobes and in some cases have identified species in their ionized form, such as O^+, Al^+, Si^+, and possibly P^+, that have not been observed in their corresponding neutral form [*Hilchenbach et al.*, 1993; *Mall et al.*, 1998; *Yokota et al.*, 2009; *Tanaka et al.*, 2009; *Poppe et al.*, 2012; *Halekas et al.*, 2012, 2013].

[4] While a majority of pickup ion observations at the Moon and other small airless bodies occur in the solar wind

---

[1] Space Sciences Laboratory, University of California, Berkeley, California, USA.
[2] NASA Lunar Science Institute, Ames Research Center, Mountain View, California, USA.
[3] Goddard Planetary Heliophysics Institute, University of Maryland, Baltimore, California, USA.
[4] NASA Goddard Space Flight Center, Greenbelt, Maryland, USA.

Corresponding author: A. R. Poppe, Space Sciences Laboratory, University of California, 7 Gauss Way, Berkeley, CA, USA. (poppe@ssl.berkeley.edu)

2169-9097/13/10.1002/jgre.20090

Table 1. A List of the Parameters in the Pickup Ion Tracing Model

Variable	Description	Constraint or Source
B	Magnetotail lobe magnetic field (nT)	Directly measured by ARTEMIS
v_c	Magnetotail convection speed (km/s)	Fit to ARTEMIS PUI energy spectra[a]
θ_c	Convection angle (from $+Y$ SSE) (degrees)	Fit to ARTEMIS PUI angular spectra
ϕ	Maximum photoelectron sheath potential (V)	Previous in situ measurements [*Reasoner and Burke*, 1972]
λ_D	Photoelectron sheath thickness (km)	Previous in situ measurements [*Reasoner and Burke*, 1972]
m	Ion mass (amu)	Free parameter in model
H_g	Neutral exospheric scale height (dependent on ion mass) (km)	Previous exospheric observations [*Potter et al.*, 2000]
α	Neutral exospheric solar zenith angle exponent ($n \propto \cos^{\alpha}\theta$)	Free parameter
θ_e	Exospheric angular offset from subsolar point	Fit to ARTEMIS PUI spatial distribution

[a] PUI = pick-up ion.

where the large convection velocity provides a relatively strong convection electric field, ions will be "picked-up" any time there is a convecting magnetic field. This has been demonstrated by recent observations reported by both the KAGUYA and Acceleration, Reconnection, Turbulence and Electrodynamics of the Moon's Interaction with the Sun (ARTEMIS) spacecraft around the Moon in the terrestrial magnetotail lobes [*Tanaka et al.*, 2009; *Poppe et al.*, 2012], which provide excellent opportunities to study lunar pickup ions due to both the steady magnetic field and relatively quiet background plasma environment. In the magnetotail, typical convection speeds for geomagnetically quiet times can be more than an order-of-magnitude less than in the solar wind [*Troshichev et al.*, 1999], and thus, it becomes important to not only consider the convection electric field but also the lunar surface electric field generated through solar ultraviolet-stimulated photoemission [*Reasoner and Burke*, 1972]. Indeed, while solar wind observations can make use of theoretical machinery to relate observed pickup ion observations to source ion densities, and in turn, neutral densities [*Yokota and Saito*, 2005; *Hartle and Killen*, 2006; *Halekas et al.*, 2013], a particle modeling approach is necessary to account for both convection and surface electric fields.

[5] In this paper, we present a comparison of previously reported ARTEMIS observations of lunar pickup ions in the terrestrial magnetotail with an ion particle-tracing model assuming the ions result from photoionization of the lunar neutral exosphere. In section 2, we describe the model used to investigate the dynamics of lunar pickup ions and present several features predicted by the model. In section 3, we compare the detailed features of the ARTEMIS pickup ion observations in the tail lobes in order to constrain as many parameters for each observation as possible. Using the constraints derived in section 3 and calculated photoionization rates, section 4 presents upper limits on the neutral density of an array of species either known or likely to be found in the lunar exosphere. Finally, in section 5, we discuss the implications of these results and outline future work.

2. Model Description and Results

[6] We use a particle-tracing model to investigate the behavior and distribution of lunar pickup ions in the terrestrial magnetotail lobes in an effort to use previously reported ARTEMIS observations of pickup ions in the tail lobes [*Poppe et al.*, 2012] to constrain the distribution and density of the lunar exosphere. The model is set in the Solar Selenocentric Ecliptic (SSE) coordinate frame, with the X axis along the Sun-Moon line, the Z axis toward ecliptic north, and the Y axis completing the set. The particle-tracing model includes the following:

[7] 1. the background tail lobe magnetic field, **B** (directly measured by the ARTEMIS spacecraft). The magnetic field is kept steady throughout the entire simulation. We note that while plasma sheet crossings in the magnetotail will be accompanied by highly variable magnetic fields, the magnetic field in the tail lobe at the Moon is steady over tens of hours, i.e., much long than a typical ARTEMIS flyby [*Poppe et al.*, 2012]. In addition, comparisons to ARTEMIS pickup ion observations in the tail lobes are made during steady magnetic field conditions;

[8] 2. the electric field induced from the convection of the tail magnetic field, $\mathbf{E_c} = -\mathbf{v_c} \times \mathbf{B}$, where $\mathbf{v_c}$ is the convection velocity. Typical convection velocities in the distant magnetotail during geomagnetically quiet times range between 10 and 50 km/s [*Troshichev et al.*, 1999] in the Y-Z SSE plane, perpendicular to the background magnetic field. We choose to parameterize the convection velocity by a magnitude, v_c, and an angular rotation, θ_c, from the $+Y$ SSE axis in the Y-Z SSE plane. When comparing to specific ARTEMIS pickup ion observations, we constrain the magnitude of the convection velocity (and hence, the convection electric field) by comparing the model to the observed ion energy spectra;

[9] 3. the photoelectric field above the lunar surface, $\mathbf{E_{ph}}(\mathbf{r}) = E_o \exp(-r/\lambda_D)\cos\theta\ \hat{\mathbf{r}}$, where E_o is the magnitude of the photoelectric field at the subsolar surface point, r is the radial distance above the lunar surface, λ_D is the local Debye length, θ is the angle from the subsolar axis ($+X$ SSE), and $\hat{\mathbf{r}}$ is the radial unit vector. The magnitude of the electric field is estimated using the form, $E_o = \phi/\lambda_D$, where ϕ is the lunar surface potential with respect to infinity. Previous Apollo-era observations have shown that the lunar surface potential in the magnetotail falls in the range between +40 and +200 V [*Reasoner and Burke*, 1972]. While ambient conditions in the tail lobe may drive the surface potential to vary within this range, we adopt a value of $\phi = +100$ V for this modeling;

[10] 4. an exospheric neutral distribution, $n_n(r,\theta)$, that serves to weight the initial position of the ions. We adopt a *Chamberlain* [1963]-type model,

$$n_n(r,\theta) = n_o \exp\left(-r/H_g\right)\cos^{\alpha}(\theta - \theta_e), \tag{1}$$

where n_o is the density at the subsolar surface point, H_g is the exospheric scale height, α is the exponent governing the neutral angular distribution, and θ_e is a possible bulk angular

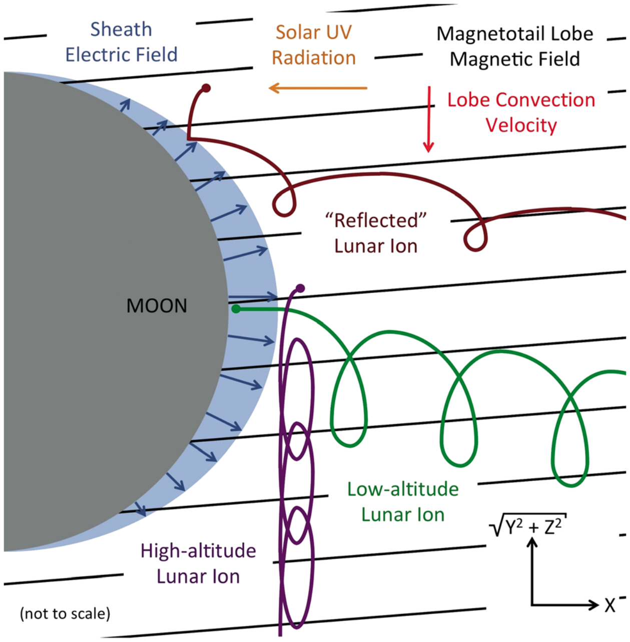

Figure 1. A cartoon of the dynamics of lunar pickup ions in the terrestrial magnetotail, updated from *Poppe et al.* [2012] to include ions that scatter off of the lunar dayside photoelectron sheath (dark red).

offset of the neutral distribution from the subsolar point. The scale height is determined from the ion mass, m_i, the neutral temperature, T_n, and the lunar gravitational constant, $g = 1.6\,\mathrm{m/s^2}$, according to $H_g = kT_n/m_i g$. We consider $\alpha = [0,1,2]$ which ranges from an isotropic neutral distribution ($\alpha = 0$) to a more peaked distribution ($\alpha = 2$). While specific exospheric production processes are expected to generate neutral distributions with $\cos\theta$ or $\cos^2\theta$ angular dependence, we include all three values of α for completeness. The exospheric offset angle, θ_e, is included to allow for the possibility that the source neutral distribution is not centered on the subsolar point. While photon-stimulated desorption and solar wind bombardment will tend to produce an exosphere centered on the subsolar point, micrometeoroid bombardment, a dominant production mechanism of the exosphere in the magnetotail [*Sarantos et al.*, 2008], is known to have distinct directional anisotropies [*Janches et al.*, 2006; *Poppe et al.*, 2011], which may lead to a bulk angular offset in the neutral exosphere. We explore the role of such an offset in reproducing the ARTEMIS pickup ion spectra later in section 3.

[11] Given the dayside location of the observed pickup ions, we do not include any nightside or terminator surface electric fields. Additionally, we do not include the presence of any crustal magnetic fields. The ions are integrated in time with the position and velocity reported out at regular intervals until they either leave a $10\,R_L$ box centered on the Moon or impact the lunar surface. A typical model run consists of 25,000 individual ions run for a specific set of conditions. Table 1 summarizes the various parameters available in the model as well as the constraint provided by either the ARTEMIS data (for a specific observation) or previous measurements or theory for each parameter.

[12] Figure 1 shows a cartoon updated from *Poppe et al.* [2012] of the various fields and quantities relevant for the modeled pickup ions. The ions can be grouped into three general categories based on their interaction with the ambient

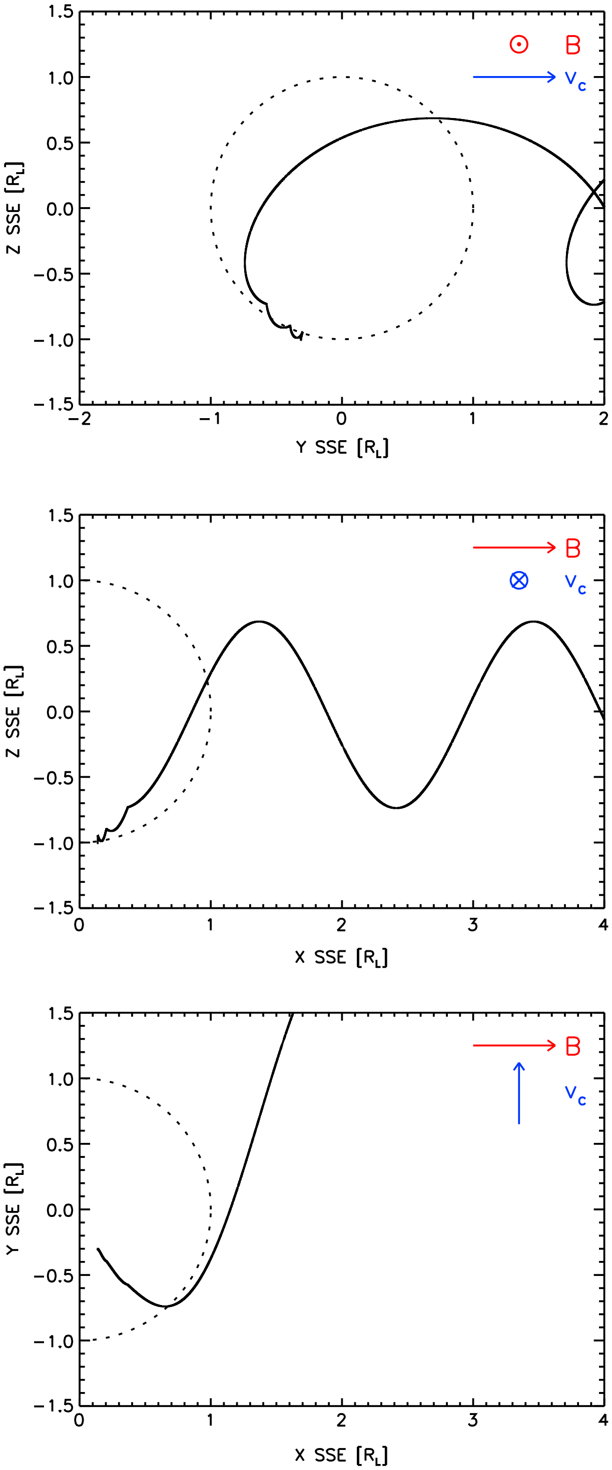

Figure 2. An example pickup ion undergoing repeated bounces off of the lunar photoelectron sheath in the magnetotail lobes. The panels show the (top) *Y-Z*, (middle) *X-Z*, and (bottom) *X-Y* planes, respectively, with the magnetic field and convection velocity marked on each panel in red and blue, respectively.

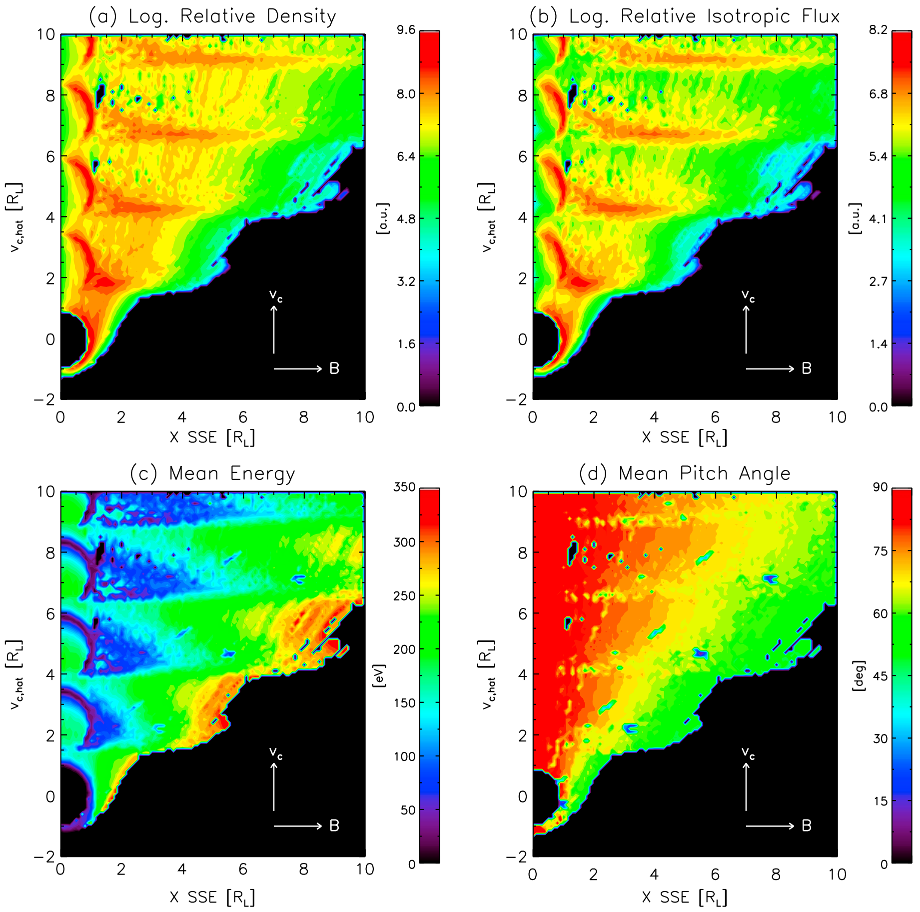

Figure 3. The (a) relative density, (b) relative isotropic flux, (c) mean energy, and (d) mean pitch angle of lunar exospheric pickup ions in the magnetotail lobe. For this example, we use mass 26 ions with a magnetic field, $B = [8,0,0]$ nT, convection speed, $\mathbf{v_c} = [0, 20, 0]$ km/s, surface electrostatic potential and sheath thickness, $\phi = +100$ V and $\lambda_D = 0.5$ km, respectively, and a neutral exospheric distribution proportional to $\exp\left(-z/H_g\right)\cos^2\theta$, where θ is the solar zenith angle and $H_g = 75$ km is the scale height.

electric fields: (a) Those ions born at high altitudes above the Moon that interact only with the convection electric field ("high-altitude" ions in purple), (b) ions born at low altitudes within the photoelectron sheath that interact with both sheath electric and convection electric fields ("low-altitude" ions in green), and (c) ions that, while born at high altitudes outside of the lunar photoelectron sheath, are initially on trajectories that intersect the Moon and thus also interact with both the surface and convection electric fields ("reflected" ions in dark red). The ions are reflected off of the lunar dayside, which continues until the ions are either on a trajectory that does not intersect the Moon or when the ion gains enough energy to overcome the photoelectron sheath potential and impact the surface. Figure 2 illustrates the behavior of a reflected pickup ion, showing three different projections of the trajectory of a single ion as it scatters multiple times off of the lunar photoelectron sheath and eventually onto a trajectory away from the Moon. Notably, as this example shows, reflected pickup ions will gain parallel components of velocity and thus travel at pitch angles other than 90°, a distinct feature noted in previously reported observations [*Poppe et al.*, 2012]. Indeed, as we will show, the reflected pickup ions form a significant component of the pickup ion flux on the dayside lunar surface while in the terrestrial magnetotail.

[13] Figure 3 shows results from an example model run with 25,000 ions initialized in a Monte Carlo fashion above the lunar surface as described earlier. For this example, we used an ion mass of 26 amu (used as a proxy for species with masses between that of Na^+ and CO^+), $\mathbf{B} = [8,0,0]$ nT, $\mathbf{v_c} = [0,20,0]$ km/s, $\phi = +100$ V, $\lambda_D = 0.5$ km, and $H_g = 75$ km. Figures 3a, 3b, 3c, and 3d show the relative density, isotropic flux, mean energy, and mean pitch angle, respectively, of the pickup ion plume within 0.1 R_L of the plane containing the X SSE axis and the convection velocity. These values are calculated by summing over the individual particle contributions to the density, flux, energy, and pitch angle with each trajectory appropriately weighted for the chosen exospheric distribution based on the particle's starting position. In this case, the magnetic field is pointing horizontally (toward the Sun) while the convection velocity is upwards. The pickup ions drift along with the convection velocity, with an additional dispersion in the sunward direction induced by the presence of the lunar photoelectric field, resulting in a broad wedge of pickup ions off one side of the dayside lunar surface. The density, isotropic flux, and mean energy have a repeating spatial structure in the direction of the convection velocity at intervals given by $2\pi r_L$, where r_L is the ion Larmor (gyro-) radius (for this example, $r_L = 0.39$ lunar radii) [*Cladis et al.*, 1994].

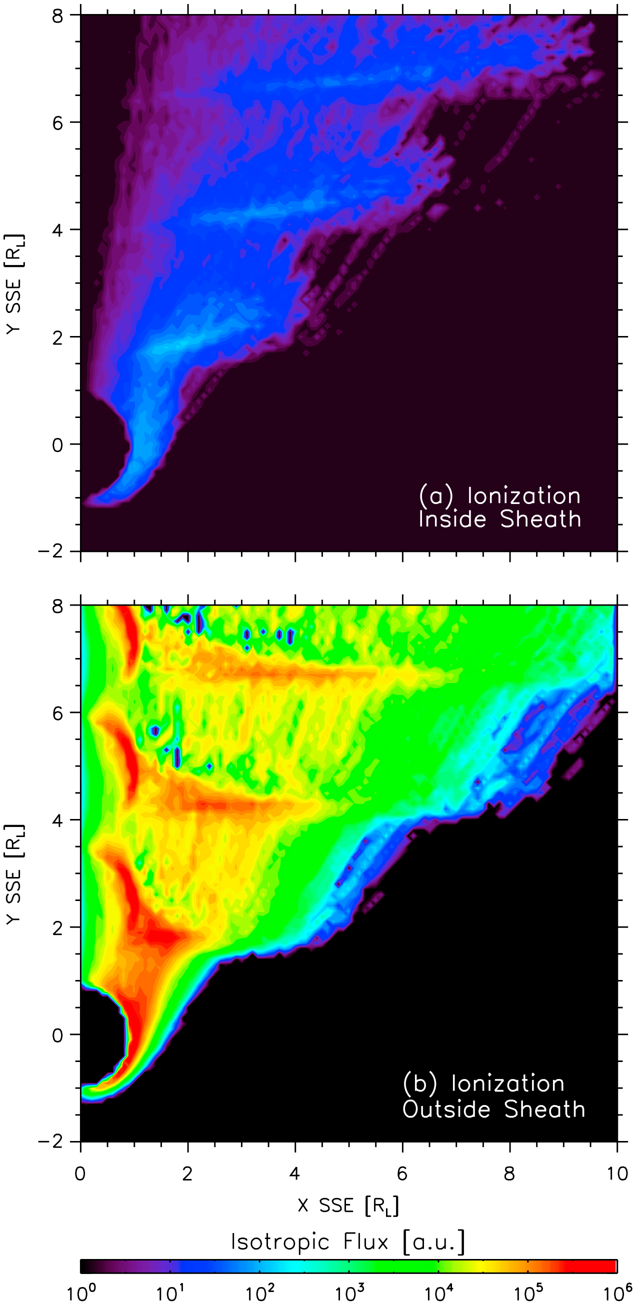

Figure 4. The isotropic flux for the same conditions as modeled in Figure 5a, with the ions divided by source region: (a) only ions born within the photoelectron sheath region and (b) only ions born outside of the photoelectron sheath region. Although arbitrary in magnitude, the color scale is appropriately normalized between the two cases.

Ions with no acceleration from the photoelectron sheath form the bulk of the pickup ion density and isotropic flux in a repeating semi-circular imprint drifting solely in the convection direction away from the Moon. Ions with parallel acceleration contribute to the series of horizontal ridges that, while repeating at the same spatial distance along the convection direction, also disperse along the magnetic field lines due to the spread in parallel velocities. The semi-circular structure propagating vertically in the mean energy results from the characteristic velocity along a pickup ion cycloid trajectory, where the maximum velocity and energy are obtained at the "top" of the cycloid (at a horizontal distance of πr_L) while the minimum velocity and energy occur in the cusp (at $2\pi r_L$). Additionally, the mean energy shows a series of ridges dispersing along the field lines again resulting from the convolution of the perpendicular convection motion and the parallel sheath velocity. Finally, the mean pitch angle of the pickup ion plume shows expected behavior, varying from 90° directly along the convection direction (and by definition, perpendicular to the magnetic field) to approximately 45° for ions that gain the greatest amount of parallel velocity.

[14] To further quantify the role that the photoelectron sheath plays in generating pickup ions with non-90° pitch angle pickup ions, we ran the model with 25,000 ions under the same set of conditions as shown in Figure 3 but divided the ions into two groups based on whether they were born outside the sheath (defined as greater than five Debye lengths from the surface, at which point the photoelectric field is negligible) or within the sheath. Figures 4a and 4b show the isotropic flux for ions born within and outside of the sheath, respectively. The color scales for both panels are correctly normalized to each other. In Figure 4a, the ions born within the photoelectron sheath gain both parallel and perpendicular velocities resulting in the wedge of flux trailing off the side of the Moon, as expected. In Figure 4b, the flux consists not only the plume of ions drifting along the convection direction (+*Y* SSE in this example) but also a wedge of ions similar to the flux produced from ions born in the sheath. Indeed, the flux produced by the ions which reflect off of the photoelectron sheath, and gain parallel energy is several orders-of-magnitude greater than the flux from ions born within the sheath. This effect should be limited to cases in which convection is rather weak, such as in the tail lobes, where the convection electric field cannot accelerate pickup ions to energies greater than the photoelectron sheath potential. We do not expect such an effect in the solar wind, for example, where the photoelectric sheath potential of approximately +5–10 V [*Freeman and Ibrahim*, 1975; *Poppe and Horányi*, 2010] is far less than the keV and greater energies typically achieved by pickup ions in the solar wind [*Halekas et al*., 2012, 2013].

[15] While much of the pickup ion behavior in the tail lobes is symmetric about the *X* SSE axis, the orbital trajectories of the twin ARTEMIS spacecraft must be accounted for in interpreting the measurement, or lack thereof, of lunar pickup ions. Both of the ARTEMIS probes orbit in highly elliptical, near-equatorial orbits that precess pro- and retrograde for P1 and P2, respectively [*Angelopoulos*, 2010; *Sibeck et al*., 2011]. One of the dominant factors in determining whether or not the ARTEMIS probes observe pickup ions in the tail lobes in the direction of the convection velocity, θ_c, defined as the angle from the +*Y* axis in the *Y*-*Z* SSE plane. As pickup ions by nature drift with the convection velocity, any periods where the convection velocity lies significantly out of the ARTEMIS probes' orbital planes will tend to reduce the chance of observation. To demonstrate this, Figure 5 shows the isotropic flux for pickup ions under the same conditions as presented in Figures 3 and 4, but for three different convection angles: (a) $\theta_c = 0°$, similar to Figure 3a, (b) $\theta_c = 45°$, and (c) $\theta_c = 90°$. On each panel, we also plot the trajectories of ARTEMIS P2 on 13 October 2011 and

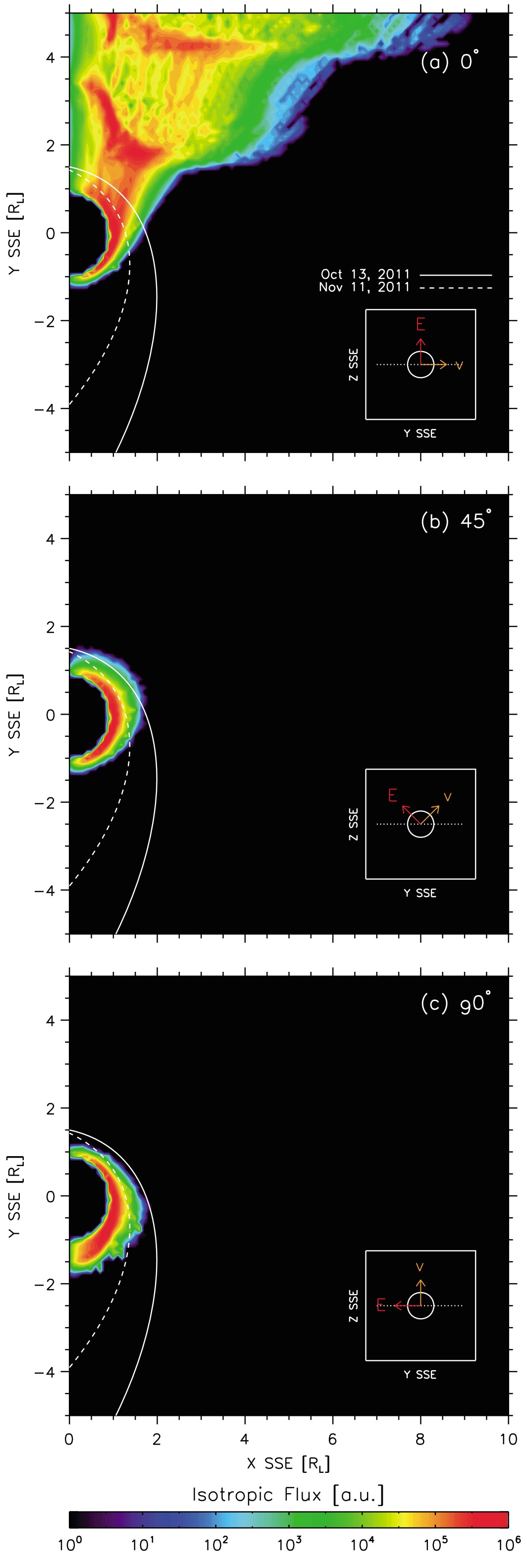

Figure 5. The isotropic flux for the same conditions modeled in Figure 3, with the convection velocity and electric field in three different directions: (a) unrotated (0°), (b) rotated 45°, and (c) rotated 90°. In all three panels, the ARTEMIS P2 orbits on 13 October 2011 and 11 November 2011 are shown for comparison. Additionally, the inset in the lower left corner of each panel shows a view of the convection velocity and electric field in the *Y-Z* SSE plane, for reference.

11 November 2011 for reference, as we have previously reported on ARTEMIS P2 observations of pickup ions in the tail lobes on these dates [*Poppe et al.*, 2012]. In Figure 5a, for which the convection velocity is entirely in the $+Y$ SSE direction, the pickup ions form a broad plume in the *X-Y* SSE plane. Under this condition, the ARTEMIS probes on both days presented would have flown through a particularly intense portion of the pickup ion plume near the lunar surface. Indeed, under pure Y convection (plus or minus), almost any orbital phase of the ARTEMIS probes would suffice to offer an opportunity along some portion of the orbit to measure lunar pickup ions. In both the 45° and 90° cases, the pickup ion flux in the equatorial plane is limited to a region within approximately one lunar radius on the lunar dayside as the pickup ions quickly convect up and out of the ARTEMIS orbital plane. In the 45° case, both dates would have flown through some portion of the pickup ion flux, with the 11 November date recording slightly higher levels of flux given its lower periselene. In contrast, the 90° case would restrict observations to only the 11 November date, as the 13 October trajectory circled just outside the region of flux. While these two dates are presented only as possible orbits, they nonetheless illustrate the sensitivity of ARTEMIS pickup ion observation possibilities in the magnetotail on the angle between the convection velocity and the ARTEMIS orbital plane.

3. Comparison to ARTEMIS Data

[16] We wish to forward-model the previously reported ARTEMIS measurements and in doing so, constrain the physical quantities involved including the convection velocity, exospheric distribution, and neutral densities. The observation that we discuss here was taken by the ARTEMIS P2 spacecraft on 11 November 2011 while the Moon passed through the terrestrial magnetotail lobes. We also performed the analysis described below for the other lobe pickup ion observation described in *Poppe et al.* [2012] (taken on 13 October 2011) and achieved nearly identical results. Additionally, we note that other unreported pickup ion observations in the tail lobe exist in the ARTEMIS data set, which may provide for future data model comparisons looking at the pickup ion flux from an ensemble standpoint. While a full description can be found in *Poppe et al.* [2012], Figure 6 shows a summary of the 11 November 2011 ARTEMIS pickup ion observation. Figure 6a shows the position of the Moon in the Earth-centered GSE coordinate system, with typical locations of the terrestrial bow shock and magnetopause as solid and dotted lines, respectively. Figure 6b shows the ARTEMIS P2 trajectory above the dayside lunar surface where the pickup ions were observed. Figures 6c–6f show the ARTEMIS-measured magnetic field components, ion energy spectra, ion pitch angle spectra, and ion density, respectively, as a function of the Y SSE position of the ARTEMIS spacecraft. The ion density is calculated by integrating over the measured ion distribution function as described in detail in *McFadden et al.* [2008] and assumes that the measured ions are protons, since ARTEMIS electrostatic analyzer (ESA) does not make compositional measurements. Therefore, in order to compare between the ARTEMIS measurements and the model for heavy ions, we weight all the model calculations by the same misinterpreted

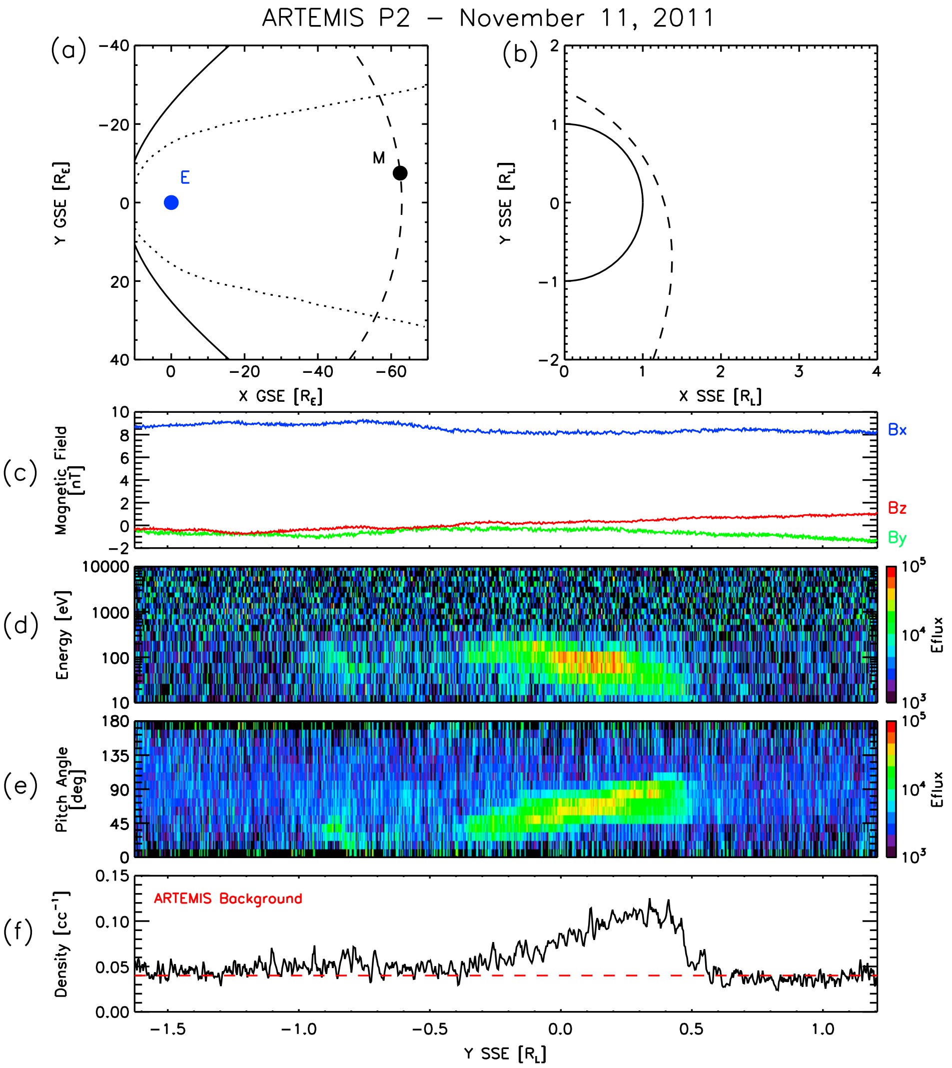

Figure 6. A summary of the ARTEMIS P2 lunar pickup ion observations in the terrestrial magnetotail. (a) The position of the Moon ("M") in the Earth's ("E") magnetotail. The solid and dotted lines represent typical locations of the bow shock and magnetopause, respectively. (b) The ARTEMIS P2 trajectory (dashed line) above the dayside lunar surface. (c–f) The magnetic field components, ion energy spectra, ion pitch angle spectra, and ion density, respectively, as a function of Y SSE location across the dayside lunar surface. Units of energy flux are in eV/cm^2/str/s/eV.

factor ($1/\sqrt{m_i}$, where m_i is the heavy ion mass), as described in further detail below. ARTEMIS observed a very short and faint burst of pickup ions centered around $-0.9\,R_L$ followed by a broader plume of pickup ions ranging from approximately -0.5 to $0.5\,R_L$. The ions of interest for this study are the latter burst (the smaller burst is discussed in greater detail in *Poppe et al.* [2012] and is not considered further here).

[17] To make a direct comparison between the observed and modeled spectra, we first run the model for a given set of parameters to produce three-dimensional energy and pitch angle fluxes on a $0.1\,R_L$ grid encompassing the lunar dayside region. The ARTEMIS trajectory corresponding to a specific orbit is then traced through the model distributions, and synthetic time series are constructed by interpolating from the model grid to the ARTEMIS trajectory. The interpolation accounts for the spacecraft potential (typically about +40 V in the tail lobes) which retards ions as they enter the electrostatic analyzer (ESA) instrument and the misinterpretation of heavy ion densities and fluxes due to the lack of ion composition measurements [*McFadden et al.*, 2008]. The modeled differential energy and angular fluxes are then de-resolved down to the ARTEMIS ESA resolutions for direct comparison. (We note that as described in *McFadden et al.* [2008], the energy and angular response of the ARTEMIS ESA anodes are corrected for the finite energy and angle response, ensuring valid comparisons between the ARTEMIS data and the model.) Through our investigation with the model, we found that the observed energy and pitch angle spectra are discriminators on several of the model parameters. Indeed, simple visual inspection of the synthetic spectra can effectively constrain the convection speed and convection angle.

[18] As an example of how the spectra can be used to discriminate against the variables in the model, Figure 7 shows a comparison between the ARTEMIS P2 pickup ion energy and pitch angle spectra from 11 November 2011 (first row) [*Poppe et al.*, 2012] and four model cases (second, third,

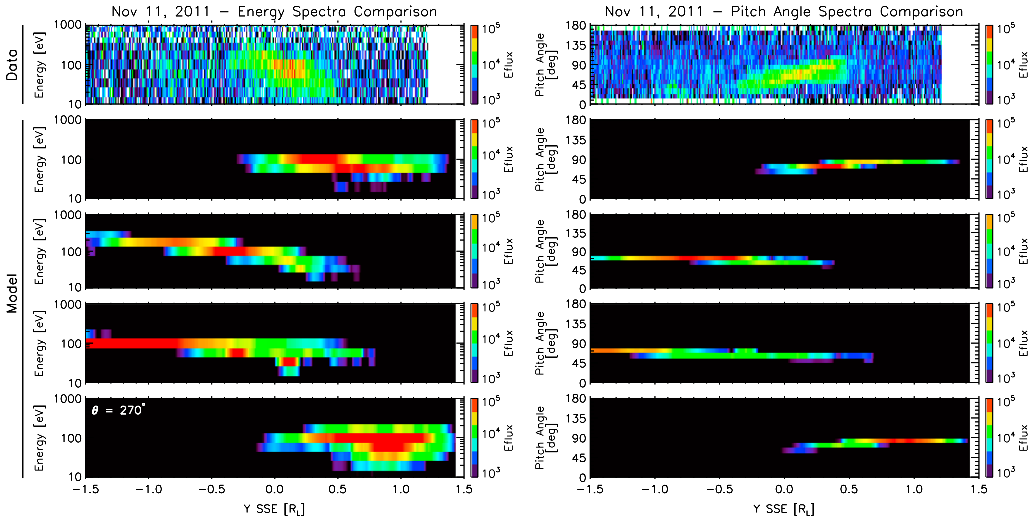

Figure 7. A comparison of ARTEMIS P2 and model-based energy and pitch angle spectra for 11 November 2011 with varying convection angles.

fourth, and fifth rows) with identical simulation parameters except the direction of the convection velocity in the Y-Z SSE plane. This simulation series used an ion mass of 42 amu, a convection velocity of 30 km/s, $\mathbf{B}=[8,0,0]$ nT, and an electrostatic sheath potential of +100 V. The four model panels show the energy and pitch angle spectra with the convection velocity rotated by angles, $\theta_c=0°$, 90°, 180°, and 270° from the $+Y$ SSE axis. We immediately observe that the spectra for $\theta_c=90°$ and 180° disagree with the observed ARTEMIS spectra. Under both these cases, the model predicts an extensive plume of pickup ions on the $-Y$ SSE side of the Moon (dawnside), which is distinctly not seen in the ARTEMIS spectra. Additionally, the pitch angle spectra for 90° and 180° convection angle disagree with the observed pitch angle spectra, with the model spectra having decreasing pitch angle as the spacecraft heads in the $+Y$ SSE direction. In contrast, the 0° and 270° cases predict pickup ion plumes off the $+Y$ SSE side of the Moon, similar to that of the ARTEMIS measurements; however, the pitch angle spectra allow us to further rule out the 270° case as the model predicts the pickup ions to appear almost exclusively at 90°, while the 0° case most closely matches the increasing pitch angle dispersion seen in the ARTEMIS data. Putting together the energy and pitch angle spectra, the model indicates that under these conditions, convection angles ranging from approximately 90° to 270° can be ruled out. Of the four convection angles shown, the 0° case most closely resembles the ARTEMIS observations on this date for the parameters chosen. We note that the agreement between the 0° case and the ARTEMIS data are not complete; indeed, as we will show later in Figure 9, the best fit convection angle is at approximately 30°, implying magnetotail convection in the $+Y$ and $+Z$ SSE directions.

[19] We also explored the role that the photoelectron sheath strength played in determining the pickup ion distributions and found that for the parameter regime present in the magnetotail, the distributions are only weakly dependent on changes in the specific photoelectron sheath values. The lunar surface potential in the magnetotail lobes is somewhat uncertain, with the only in situ measurement coming from the Charged Particle Lunar Environment Experiment (CPLEE) deployed on the lunar surface by the Apollo 14 mission [*Reasoner and Burke*, 1972]. CPLEE measurements indicated that during geomagnetically quiet times, the lunar surface potential in the magnetotail lobes was in the range of +40 to +200 V. Given surface potentials of this magnitude, one can compute the distance through which a pickup ion must be accelerated by the magnetotail electric convection field in order to obtain energies capable of overcoming the surface potential. In contrast, those ions that do not overcome the surface electrostatic potential are represented in Figure 1 as the "Reflected lunar ions." For example, a 30 km/s convection speed in an 8 nT lobe field (both typical values) yields a convection electric field of approximately 0.25 mV/m. In this convection field, a pickup ion must be accelerated through 200 km in order to obtain an energy of 50 eV. This distance is greater than or comparable to scale heights for most exospheric species, implying that a significant fraction of any species in the lunar exosphere resides too close to the Moon to gain enough energy from pickup acceleration to overcome the electrostatic sheath barrier and are therefore reflected from the lunar surface electric field. This scaling holds for the majority of the lunar exosphere, although there are exceptions. The sheath potential is typically weaker toward the terminators, which would allow more pickup ion flux to overcome the electrostatic barrier in this region. Also, nonthermal exospheric distributions, such as the extended lunar Na and K coronae [*Mendillo et al.*, 1991], will produce pickup ions at sufficient distance from the Moon to be accelerated to energies capable of overcoming the sheath. Nevertheless, for the bulk of most species, even relatively low lunar surface potentials (> +10 V) are sufficient to reflect a large fraction of the pickup ion flux in the magnetotail.

[20] In order to derive neutral density limits on species in the lunar exosphere, we chose four masses to represent the most likely constituents which conveniently fall into four roughly similar mass bins. The two leftmost columns of Table 2 list these species and their masses, grouped by simulation mass. The model used masses 15, 26, 42, and 56 amu to represent the four groups. For each simulated mass, we

Table 2. Photoionization Rates, Previous Upper Limits to the Density, and Limits Derived in This Work for a Range of Pickup Ion Species Expected at the Moon

Species	Mass (amu)	Photoionization Rate (s^{-1})[a]	Previous Upper Limit (cm^{-3})[b]	Minimum Upper Limit Presented Here (cm^{-3})
C	12	8.75×10^{-7}	< 200	< 2500
N	14	4.4×10^{-7}	< 600	< 7250
O	16	4.57×10^{-7}	< 500	< 9600
CH_4	**16**	**5.9×10^{-7}**	**$< 10^4$**	**< 7500**
OH	**17**	**6.43×10^{-7}**	**$< 10^6$**	**$< 8 \times 10^3$**
Na	23	1.6×10^{-5}	70	< 320
Mg	24.3	4.97×10^{-7}	< 6000	$< 1.2 \times 10^4$
Al	**27**	**7×10^{-4}**	**< 55**	**< 10**
Si	28	4.43×10^{-5}	< 48	< 180
N_2	28	7.23×10^{-7}	800	$< 1.1 \times 10^4$
CO	28	6.95×10^{-7}	< 1000	$< 1.1 \times 10^4$
K	39	2×10^{-5}	17	< 550
Ca	40	7.8×10^{-5}	< 1	< 150
Ar	**40**	**6.1×10^{-7}**	**10^5**	**$< 1.9 \times 10^4$**
CO_2	44	1.22×10^{-6}	< 1000	$< 1.1 \times 10^4$
Fe	56	3.7×10^{-6}	< 380	$< 5 \times 10^4$

Rows in bold represent improvements on previous upper limits.

[a] *Huebner et al.* [1992].

[b] *Stern* [1999, and references therein].

ran a series of simulations over a wide range of convection speeds and angles, and using the visual inspection process described earlier, we determined the best fit pair of convection speed and direction for each mass. Naturally, as the mass increased, the best fit convection speed decreased; in contrast, the best fit convection direction had only very weak mass dependence. Depending on the mass simulated, the best fit convection speed ranged from approximately v_c = 35–55 km/s, consistent with previous observations of convection speeds in the distant magnetotail [*Troshichev et al.*, 1999]. Additionally, we found convection predominantly in the +*Y* SSE direction, at an angle of $\theta_c = 30°$, again consistent with typical dawn-to-dusk convection in the magnetotail [*Troshichev et al.*, 1999].

[21] Additionally, we also used the model to explore the existence of a bulk angular offset, θ_e, in the neutral exospheric distribution, which could be indicative of the relative strength of various neutral production mechanisms, assuming that the neutrals are $\cos^2\theta$ distributed in solar zenith angle (i.e., $\alpha = 2$). Figure 8 shows a comparison of the ARTEMIS pickup ion density on 11 November 2011 and the model-predicted pickup ion density as a function of distance across the lunar dayside for a series of six exospheric offset angles. In Figure 8a, the ARTEMIS data (black) show a gently rising peak in ion density above the instrument background (dashed line) beginning at approximately $-0.3\,R_L$ of the lunar subsolar point, following by a sharp decline at $+0.5\,R_L$. On an identical scale, Figure 8b shows densities for a single model run with the exospheric offset angle varying from 0° to −75° which represents an angular exospheric offset toward the dawn terminator. In the case of no exospheric offset (purple), the model-predicted pickup ion density extends far to the +*Y* SSE direction of the observed plume. Rotations of the neutral exosphere by 15° increments translate the model density in the −*Y* SSE direction and narrow the predicted plume, with the extreme case of −75° offset (red) predicting a very narrow peak far to the dawnside of the observed peak. Intermediate offset angles can be seen to agree more closely with the observed peak. Indeed, Figure 8c shows the comparison between the ARTEMIS observed density and the model-predicted pickup ion density with exospheric offset angles of $\theta_e = 0°, -37°$, and $-75°$. In this case, the model density with $\theta_e = -37°$ agrees best with the observation, showing both the gradual rise in density followed by the sharp decline.

[22] With the exospheric offset of $\theta_e = -37°$ built into the model, we can compare both the ARTEMIS energy and angular spectra to determine the overall quality of the fit. Figure 9 shows the energy and pitch angle spectra for both the model and the ARTEMIS measurements of 11 November 2011 [*Poppe et al.*, 2012]. In this case, the model was run for mass 42 amu with convection speed 40 km/s, convection angle 30°, sheath potential +100 V (although this parameter only weakly determines the outcome), and exospheric offset angle 37°. In all three spectra, the spatial extent of the modeled pickup ion plume is restricted to mainly between −0.5 and 0.5 R_L of the lunar subsolar point and agrees well with the ARTEMIS observation. In both the energy and pitch angle flux, the model predicts flux within the observed minimum and maximum bounds; however, the flux does not reproduce the entire extent in either energy or pitch angle. The most likely explanation for this is that the observed plume consists of a combination of several different masses (cf. KAGUYA ion mass spectrometry measurements in the tail lobe) [*Tanaka et al.*, 2009; *Saito et al.*, 2010] which, under identical convection conditions, will tend to diverge in energy and pitch angle producing broader signatures in the ARTEMIS spectra.

4. Exospheric Constraints

[23] Having identified the best fit model parameters (convection speed and direction, exospheric offset, etc.) for

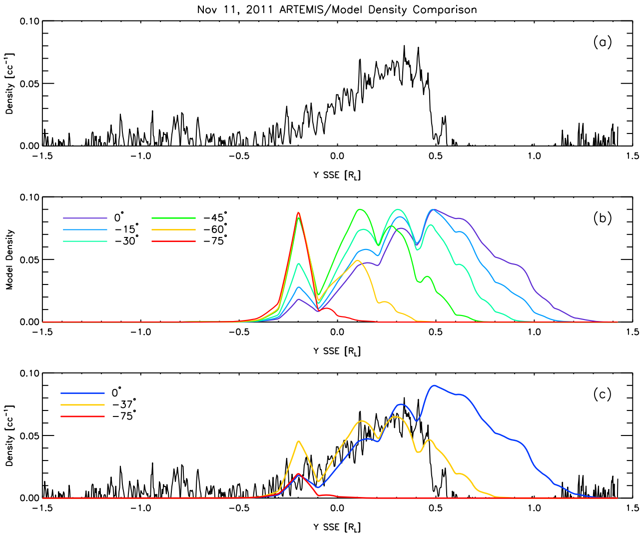

Figure 8. (a) The density of pickup ions observed along the 11 November 2011 ARTEMIS P2 trajectory with the background subtracted. (b) Model-predicted pickup ion densities for mass 42 amu ions along the same ARTEMIS trajectory for a range of exospheric offset angles. (c) A comparison of the normalized 11 November 2011 ARTEMIS P2 pickup ion density (black) with the model-predicted mass 42 pickup ion density for exospheric offsets of $\theta_e = 0°, -37°$, and $-75°$.

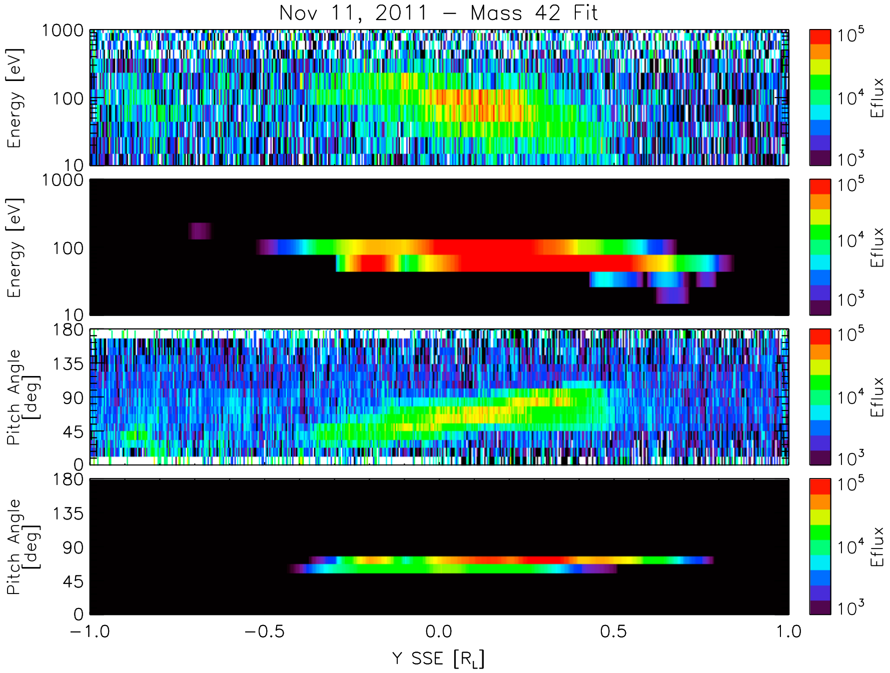

Figure 9. A comparison between 11 November 2011 ARTEMIS P2 observations and the best fit model of the pickup ion differential energy and pitch angle flux. The model was run for a single species with empirically fit parameters, as described in the text. Units of energy flux are in eV/cm^2/str/s/eV.

the ARTEMIS observation, we can now derive upper limits for the neutral density of species believed to be in the lunar exosphere. For each modeled mass, we determine the model-predicted ion density along the ARTEMIS orbit, $n_i(x,y,z)$, as a function of the total ion production rate, R_i, according to,

$$n_i(x,y,z) = \frac{R_i}{\sqrt{m_i}} \frac{T(x,y,z)}{N_i V_b}, \tag{2}$$

where m_i is the ion mass, N_i is the total number of simulated model ions, V_b is the volume of model grid cell, and $T(x,y,z)$ is the total time that all modeled ions spent in the grid cell centered at $[x,y,z]$. The total time histogram is calculated by summing over individual model ion trajectories,

$$T(x,y,z) = \frac{\sum_i w_i t_i(x,y,z)}{\sum_i w_i}, \tag{3}$$

where $t_i(x,y,z)$ is the trajectory of an individual ion and w_i is a relative weight denoting the assumed exospheric distribution as presented in equation (1). The factor of $1/\sqrt{m_i}$ in equation (2) arises from the misinterpretation of heavy ions by the ESA instrument [*McFadden et al.*, 2008]. The total ion production rate is given by,

$$R_i = R_{ph} \int \mathrm{d}V' n_n(r',\theta'), \tag{4}$$

where R_{ph} is the photoionization rate for a given species and $n_n(r,\theta)$ is the assumed exospheric distribution on the lunar dayside (equation (1)). Photoionization rates for each species are calculated by integrating atomic and molecular cross sections [*Huebner et al.*, 1992] over composite solar spectra derived from Thermosphere Ionosphere Mesosphere Energetics and Dynamics/Solar EUV Experiment and Solar Radiation and Climate Experiment/Solar Stellar Irradiance Comparison Experiment measurements on 11 November 2011 [*Woods et al.*, 2000; *McClintock et al.*, 2005]. Table 2 shows the ion mass and photoionization rates for 16 separate species thought to be in the lunar exosphere. Importantly in equation (4), the integral over the neutral density depends on n_o, T_n, and α, and absent any further constraints, the subsolar density limits derived here are temperature and α dependent. Despite not directly measuring the exospheric temperature during the ARTEMIS measurement, previous work has shown that residence in the magnetotail is correlated with a significant increase in exospheric Na temperature (approximately threefold up to a maximum around 3000 K) [*Sarantos et al.*, 2008]. The increase in Na temperature was attributed to the increasing dominance of micrometeoroid impact vaporization as the exospheric production mechanism, and thus, we expect the temperature of all exospheric species to similarly increase in the magnetotail.

[24] By combining equations (1)–(4), we solve for n_o as a function of the ARTEMIS observed ion density (with the instrument background appropriately subtracted) to determine upper limits on the subsolar neutral density. Since we do not know the composition of the observed pickup ions, our method is limited to assuming that the observed ions are a single species. We then fit an individual modeled specie to the entire observed pickup ion plume and from there, back out an upper limit on the density. Figure 10 shows the upper limits on the subsolar neutral density of six selected species (OH, Na, Al, Si, K, and Ar) in the lunar exosphere as a function of T_n for three different values of α. Both the October and November observation dates yielded similar limits. Additionally, we also show measurements or current upper limits (in the cases where no direct measurement

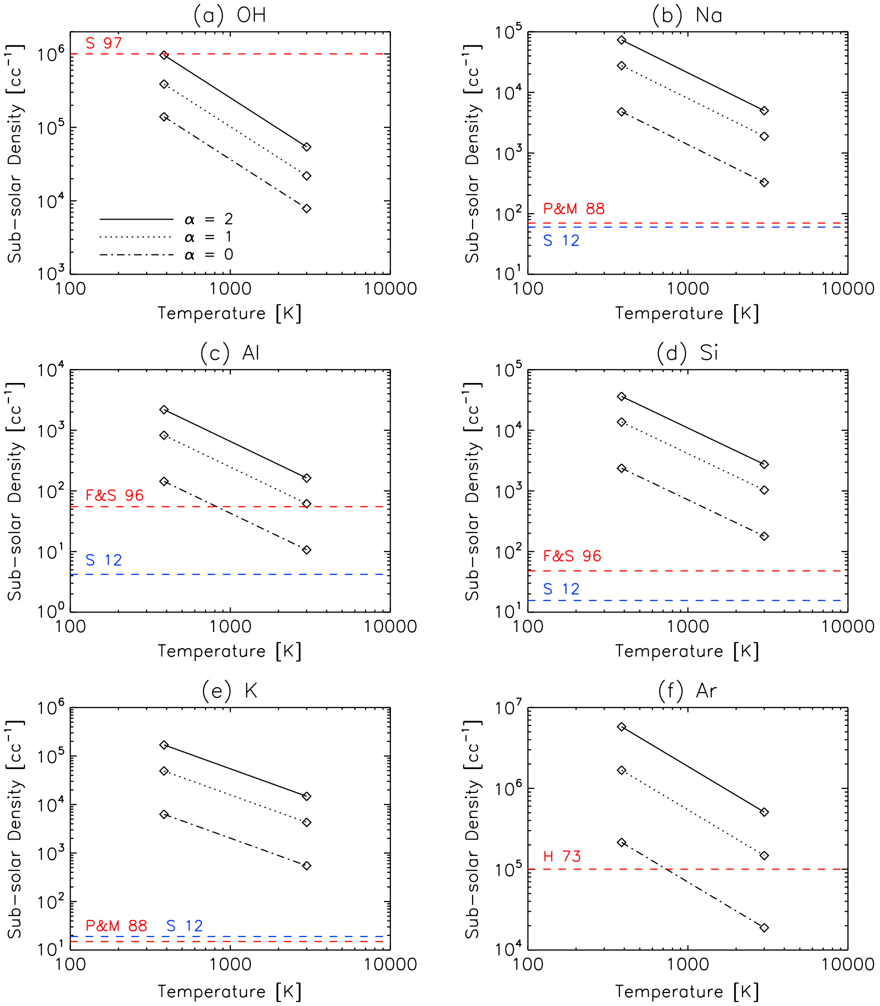

Figure 10. Constraints on the subsolar density of six lunar exospheric species from the model as a function of the neutral exospheric temperature. As labeled in the upper-left panel, the three lines present the limits assuming three different neutral angular distributions, $\cos^{\alpha}\theta$, for $\alpha = [0, 1, 2]$. The red dashed line in each panel denotes the current best upper limit on the subsolar neutral density [*Stern et al.*, 1997; *Potter and Morgan*, 1988; *Flynn and Stern*, 1996; *Hoffman et al.*, 1973]. In Na, Al, Si, and K, the blue dashed line denotes the subsolar densities due to either micrometeoroid impact vaporization or photon-stimulated desorption as predicted by the *Sarantos et al.* [2012b] model.

exists) on the neutral densities in red [*Hoffman et al.*, 1973; *Potter and Morgan*, 1988; *Flynn and Stern*, 1996; *Stern et al.*, 1997] and current model predictions for neutral densities in blue (for species for which the models are available) assuming that only micrometeoroid impact vaporization and photon-stimulated desorption operate [*Sarantos et al.*, 2012b]. For three of the species shown in Figure 10 (OH, Al, and Ar), the model provides new upper limits on the subsolar density for hotter and more isotropic ($\alpha \to 0$) neutral distributions. At its most stringent (the high temperature, isotropic case), the ARTEMIS pickup ion measurements constrain the OH density to be approximately more than 2 orders of magnitude lower, $n_{OH} < 8 \times 10^3$ cm^{-3}, the Al density to be a factor of 5 lower, $n_{Al} < 10$ cm^{-3}, and the Ar density to be a factor of 5 lower, $n_{Ar} < 2 \times 10^4$ cm^{-3}. For Si, the model does not improve upon previous limits [*Flynn and Stern*, 1996]. Additionally, Table 2 lists the best fit upper limits on the subsolar density for all species considered in the model (using values for $T_n = 3000$ K and $\alpha = 0$). These results are in good agreement with a recently published analysis of ARTEMIS pickup ion observations in the solar wind that assumed an isotropic model for exospheric neutral distributions and found similar upper limits [*Halekas et al.*, 2013]; however, we do wish to emphasize that the limits obtained here are for observations in the magnetotail, where the neutral exosphere is known to undergo significant changes [*Potter et al.*, 2000; *Sarantos et al.*, 2008; *Feldman et al.*, 2012]. One should exercise caution when comparing the numbers derived here to those found from observations in the solar wind.

[25] Regarding Na and K, for which repeated optical measurements have determined densities of $n_{Na} = 67 \pm 12$ cm^{-3} and $n_K = 15 \pm 3$ cm^{-3} [*Potter and Morgan*, 1988], the model shows that even under the most stringent limits, the Na or K subsolar neutral density required to produce the observed pickup ion flux is much higher than the known densities. In turn, this implies that Na and K do not comprise the observed pickup ions, at least at levels above the ARTEMIS background

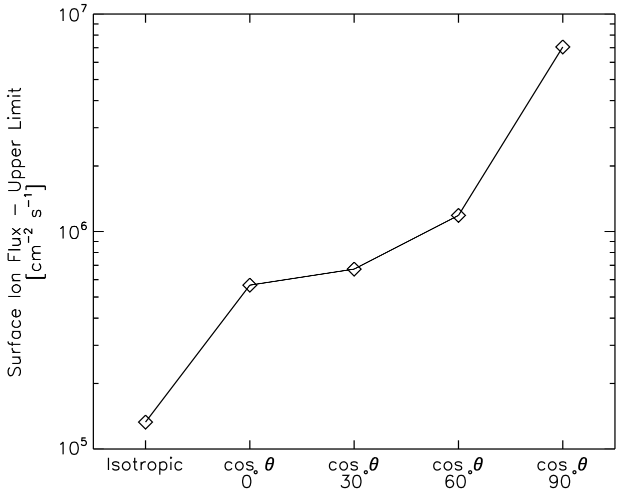

Figure 11. Constraints on the micrometeoroid bombardment-induced pickup ion flux originating directly from the lunar surface using the ARTEMIS measurements. The results are dependent on the assumed incoming micrometeoroid distribution: isotropic, and cosθ with four bulk offsets from the subsolar point toward the dawn terminator.

despite their high photoionization rates. This reasoning applies to all other species for which the previously established limits are lower than the required densities calculated here.

[26] We also note that the ARTEMIS constraints are higher than the model estimates from *Sarantos et al.* [2012b], where available (Na, Al, Si, and K), again most likely attributable to modeling the ion plume as a single species. To this end, we attempted to fit the pickup ion plume as an ensemble of multiple ion masses; however, we found the relative weights between different ion masses largely unconstrained. In contrast to the analysis done by *Halekas et al.* [2013], where the distance between the ion origin and the ARTEMIS spacecraft observation point is great enough such that different ion masses have begun to separate according to their gyroradii (and thus, appear in distinct energy and angular bins), the magnetotail pickup ion observations overlap significantly across ion mass. Therefore, in this case, we cannot quantitatively find a multi-species fit to the ARTEMIS observations. Future work may be able to identify ARTEMIS magnetotail pickup ion observations farther from the Moon than those already reported where ion species will have begun to separate, thereby allowing multi-species model constraints.

[27] As an additional exercise, we can use the model to address ions produced directly at the lunar surface via micrometeoroid bombardment [*Wekhof*, 1980]. To this end, we ran the model under identical convection parameters as above with ions generated across the dayside directly at the lunar surface. Theoretical exercises have used the incoming micrometeoroid mass flux and laboratory measurements of the charge generated upon hypervelocity impact to estimate a surface ion flux of approximately $10^3\,\mathrm{cm}^{-2}\,\mathrm{s}^{-1}$ [*Wekhof*, 1981, and references therein]; however, we are not aware of any in situ observation limits on this calculation. To constrain this flux, we forward-modeled the surface pickup ion flux using a selection of models for the incoming micrometeoroid flux: isotropic, and cosθ distributed with four bulk offset angles (similar to the bulk exospheric offset angle discussed above), 0°, 30°, 60°, and 90°, where 90° represents a micrometeoroid distribution centered on the dawn terminator. In all cases, the resulting pickup ion spectra predicted at ARTEMIS disagreed with that measured (not shown here). Thus, the ARTEMIS background count level can be used to place upper limits on the surface ion flux. Figure 11 shows upper limits derived on the micrometeoroid bombardment-induced pickup ion flux as a function of the incoming distribution, ranging from approximately $10^5\,\mathrm{cm}^{-2}\,\mathrm{s}^{-1}$ to $10^7\,\mathrm{cm}^{-2}\,\mathrm{s}^{-1}$ as the distribution shifts from isotropic to peaked at the dawn terminator. As discussed earlier, the most likely distribution at the Moon is approximately the cosθ with a 60° degree offset [*Janches et al.*, 2006], for an upper limit of approximately $10^6\,\mathrm{cm}^{-2}\,\mathrm{s}^{-1}$, significantly higher than that theoretically estimated [*Wekhof*, 1980, 1981]. Nevertheless, these constraints are, to our knowledge, the first reported from in situ. As with the exospheric pickup ions, future measurements may provide greater constraints, or in this case, even direct detection of ions produced by micrometeoroid bombardment of the lunar surface.

5. Discussion and Conclusion

[28] The model presented here has helped to illuminate several features of the lunar pickup ion flux while the Moon is in the magnetotail. Observations of lunar pickup ions in the magnetotail at pitch angles other than 90° initially prompted us to hypothesize that exospheric neutrals photoionized within the lunar photoelectron sheath constituted a major component of the lunar pickup ion flux [*Poppe et al.*, 2012]. Our modeling presented here has shown that while ions born within the sheath do gain components of parallel velocity, the main generation mechanism of non-90° pitch angle pickup ions is the electrostatic reflection of ions born from neutrals outside the sheath that are driven toward the Moon along the magnetotail convection electric field and subsequently reflected by the lunar surface electric field. Thus, in environments with relatively low convection electric fields, it is critical to include the effect of surface electric fields in interpreting pickup ion measurements. This includes not only the terrestrial magnetotail but also perhaps the magnetospheres of the outer planets, where satellites are embedded within the co-rotating planetary magnetic field. At Saturn, the Cassini spacecraft has recently observed both positive and negative pickup ions at some of the icy moons [*Teolis et al.*, 2010; *Tokar et al.*, 2012], which may interact with surface electrostatic fields [*Roussos et al.*, 2010] in similar ways to that reported here.

[29] Use of the pickup ion model has connected the ARTEMIS pickup ion measurements with the source neutral distribution. Specifically, we have shown that the pickup ion observations are best reproduced with a bulk angular offset in the neutral distribution toward the dawn terminator, which we have interpreted as the signature of micrometeoroid impact vaporization, the expected dominant production mechanism of a majority of the species in the lunar exosphere in the magnetotail [*Sarantos et al.*, 2008]. While typical models of micrometeoroid bombardment assume an isotropic influx distribution, both ground- and space-based observations have shown distinct anisotropies in the dust influx mainly due to the relative motion of the Earth-Moon system with respect to the background sporadic dust distribution

[*Janches et al.*, 2003, 2006; *Poppe et al.*, 2011]. Based on this model, one should expect the offset of the lunar exosphere to shift from a subsolar centered distribution in the solar wind to an offset distribution and back again as the Moon transits the magnetotail. Such an effect should be detectable with upcoming observations by the Lunar Atmosphere and Dust Environment Explorer (LADEE). Indeed, we look forward to detailed comparisons between simultaneous LADEE and ARTEMIS measurements of both the neutral and ionized components of the lunar exosphere in order to further constrain and validate this model.

[30] **Acknowledgments.** The authors gratefully acknowledge support from NASA's Lunar Science Institute and acknowledge NASA contract NAS5-02099 for THEMIS/ARTEMIS support. A. R. P and J. S. H. also acknowledge support from NASA's LASER program, grant #NNX13AJ97G. We thank J.P. McFadden for the use of THEMIS ESA data in support of this research. We thank the Photo-Rate Data Coefficient Data Base [http://phidrates.space.swri.edu] and the LASP LISIRD site [http://lasp.colorado.edu/lisird/missiondatafiles.html] for access to cross sections and solar spectra used to calculate photoionizations rates.

References

Angelopoulos, V. (2010), The ARTEMIS mission, *Space Sci. Rev.*, *165*(1–4), 3–25.

Chamberlain, J. W. (1963), Planetary coronae and atmospheric evaporation, *Planet. Space Sci.*, *11*, 901–960.

Cladis, J. B., W. E. Francis, and R. R. Vondrak (1994), Transport toward Earth of ions sputtered from the Moon's surface by the solar wind, *J. Geophys. Res.*, *99*(A1), 53–64.

Feldman, P. D., et al. (2012), Temporal variability of lunar exospheric helium during January 2012 from LRO/LAMP, *Icarus*, *221*, 854–858.

Flynn, B. C., and S. A. Stern (1996), A spectroscopic survey of metallic species abundances in the lunar atmosphere, *Icarus*, *124*, 530–536.

Freeman, J. W., and M. Ibrahim (1975), Lunar electric fields, surface potential and associated plasma sheaths, *The Moon*, *14*, 103–114.

Gorenstein, P., L. Golub, and P. J. Bjorkholm (1973), Spatial features and temporal variability in the emission of radon from the Moon: An interpretation of results from the alpha particle spectrometer, *Proc. 4th Lunar Sci. Conf.*, *3*, 2803–2809.

Halekas, J. S., A. R. Poppe, G. T. Delory, M. Sarantos, W. M. Farrell, V. Angelopoulos, and J. P. McFadden (2012), Lunar pickup ions observed by ARTEMIS: Spatial and temporal distribution and constraints on species and source locations, *J. Geophys. Res.*, *117*, E06006, doi:10.1029/2012JE004107.

Halekas, J. S., A. R. Poppe, G. T. Delory, M. Sarantos, and J. P. McFadden (2013), Utilizing ARTEMIS pickup ion observations to place constraints on the lunar atmosphere, *J. Geophys. Res.*, *118*, 1–8, doi:10.1029/2012JE004292.

Hartle, R. E., and R. Killen (2006), Measuring pickup ions to characterize the surfaces and exospheres of planetary bodies: Applications to the Moon, *Geophys. Res. Lett.*, *33*, L05201, doi:10.1029/2005GL024520.

Hilchenbach, M., D. Hovestadt, B. Klecker, and E. Möbius (1993), Observations of energetic lunar pick-up ions near Earth, *Adv. Space Res.*, *13*(10), 321–324.

Hoffman, J. H., and R. R. Jr.Hodges (1975), Molecular gas species in the lunar atmosphere, *The Moon*, *14*, 159–167.

Hoffman, J. H., R. R. Jr. Hodges, F. S. Johnson, and D. E. Evans (1973), Lunar atmospheric composition results from Apollo 17, *Proc. 4th Lunar Sci. Conf.*, *3*, 2865–2875.

Huebner, W. F., J. J. Keady, and S. P. Lyon (1992), Solar photo rates for planetary atmospheres and atmospheric pollutants, *Astrophys. Space Sci.*, *195*, 1–294.

Janches, D., M. C. Nolan, D. D. Meisel, J. D. Mathews, Q. H. Xhou, and D. E. Moser (2003), On the geocentric micrometeor velocity distribution, *J. Geophys. Res.*, *108*(A6), 1222, doi:10.1029/2002JA009789.

Janches, D., C. J. Heinselman, J. L. Chau, A. Chandran, and R. Woodman (2006), Modeling the global micrometeor input function in the upper atmosphere observed by high power and large aperture radars, *J. Geophys. Res.*, *111*, A07317, doi:10.1029/2006JA011628.

Mall, U., et al. (1998), Direct observation of lunar pick-up ions near the Moon, *Geophys. Res. Lett.*, *25*(20).

McClintock, W. E., G. J. Rottman, and T. N. Woods (2005), Solar Stellar Irradiance Comparison Experiment II (SOLSTICE II): Instrument concept and design, *Solar Physics*, *230*, 225–258.

McFadden, J. P., et al. (2008), The THEMIS ESA plasma instrument and in-flight calibration, *Space Sci. Rev.*, *141*(1–4), 277–302.

Mendillo, M., J. Baumgardner, and B. Flynn (1991), Imaging observations of the extended sodium atmosphere of the Moon, *Geophys. Res. Lett.*, *18*(11), 2097–2100.

Mendillo, M., B. Flynn, and J. Baumgardner (1993), Imaging experiments to detect an extended sodium atmosphere on the Moon, *Adv. Space Res.*, *13*(10), 313–319.

Poppe, A., and M. Horányi (2010), Simulations of the photoelectron sheath and dust levitation on the lunar surface, *J. Geophys. Res.*, *115*, A08106, doi:10.1029/2010JA015286.

Poppe, A., D. James, and M. Horányi (2011), Measurements of the terrestrial dust influx variability by the Cosmic Dust Experiment, *Planet. Space Sci.*, *59*, 319–326.

Poppe, A. R., R. Samad, J. S. Halekas, M. Sarantos, G. T. Delory, W. M. Farrell, V. Angelopoulos, and J. P. McFadden (2012), ARTEMIS observations of lunar pick-up ions in the terrestrial magnetotail, *Geophys. Res. Lett.*, *39*, L17104, doi:10.1029/2012GL052909.

Potter, A. E., and T. H. Morgan (1988), Discovery of sodium and potassium vapor in the atmosphere of the Moon, *Science*, *241*, 675–680.

Potter, A. E., R. M. Killen, and T. H. Morgan (2000), Variation of lunar sodium during passage of the Moon through the Earth's magnetotail, *J. Geophys. Res.*, *105*(E6), 15,073–15,084.

Reasoner, D. L., and W. J. Burke (1972), Characteristics of the lunar photoelectron layer in the geomagnetic tail, *J. Geophys. Res.*, *77*(34), 6671–6687.

Roussos, E., N. Krupp, H. Krüger, and G. H. Jones (2010), Surface charging of Saturn's plasma-absorbing moons, *J. Geophys. Res.*, *115*, A08225, doi:10.1029/2010JA015525.

Saito, Y., et al. (2010), In-flight performance and initial results of plasma energy angle and composition experiment (PACE) on SELENE (Kaguya), *Space Sci. Rev.*, *154*, 265–303.

Sarantos, M., R. M. Killen, A. Surjalal Sharma, and J. A. Slavin (2008), Influence of plasma ions on source rates for the lunar exosphere during passage through the Earth's magnetosphere, *Geophys. Res. Lett.*, *35*, L04105, doi:10.1029/2007GL032310.

Sarantos, M., R. E. Hartle, R. M. Killen, Y. Saito, J. A. Slavin, and A. Glocer (2012a), Flux estimates of ions from the lunar exosphere, *Geophys. Res. Lett.*, *39*, L13101, doi:10.1029/2012GL052001.

Sarantos, M., R. M. Killen, D. A. Glenar, M. Benna, and T. J. Stubbs (2012b), Metallic species, oxygen and silicon in the lunar exosphere: Upper limits and prospects for LADEE measurements, *J. Geophys. Res.*, *117*, A03103, doi:10.1029/2011JA017044.

Sibeck, D. G., et al. (2011), ARTEMIS science objectives, *Space Sci. Rev.*

Stern, S. A. (1999), The lunar atmosphere: History, status, current problems, and context, *Rev. Geophys.*, *37*(4).

Stern, S. A., J. W. Parker, T. H. Morgan, B. C. Flynn, D. M. Hunten, A. L. Sprague, M. Mendillo, and M. C. Festou (1997), An HST search for magnesium in the lunar atmosphere, *Icarus*, *127*, 523–526.

Stern, S. A., K. D. Retherford, C. C. C. Tsang, P. D. Feldman, W. Pryor, and G. R. Gladstone (2012), Lunar atmospheric helium detections by the LAMP UV spectrograph on the Lunar Reconnaissance Orbiter, *Geophys. Res. Lett.*, *39*, L12202, doi:10.1029/2012GL051797.

Tanaka, T., et al. (2009), First in situ observation of the Moon-originating ions in the Earth's Magnetosphere by MAP-PACE on SELENE (KAGUYA), *Geophys. Res. Lett.*, *36*, L22106, doi:10.1029/2009GL040682.

Teolis, B. D., et al. (2010), Cassini finds an oxygen-carbon dioxide atmosphere at Saturn's icy moon Rhea, *Science*, *330*, 1813–1815.

Tokar, R. L., R. E. Johnson, M. F. Thomsen, E. C. Sittler, A. J. Coates, R. J. Wilson, F. J. Crary, D. T. Young, and G. H. Jones (2012), Detection of exospheric O_2^+ at Saturn's moon Dione, *Geophys. Res. Lett.*, *39*, L03105, doi:10.1029/2011GL050452.

Troshichev, O., S. Kokubun, Y. Kamide, A. Nishida, T. Mukai, and T. Yamamoto (1999), Convection in the distant magnetotail under extremely quiet and weakly disturbed conditions, *J. Geophys. Res.*, *104*(A5), 10,249–10,263.

Wekhof, A. (1980), Ion emission from micrometeorite impacts on atmosphereless bodies, *Earth Moon Planets*, *22*, 185–189.

Wekhof, A. (1981), Negative ions in the ionospheres of planetary bodies without atmospheres, *Earth Moon Planets*, *24*(1), 45–52.

Wilson, J. K., M. Mendillo, and H. E. Spence (2006), Magnetospheric influence on the Moon's exosphere, *J. Geophys. Res.*, *111*, A07207, doi:10.1029/2005JA011364.

Woods, T. N., et al. (2000), The TIMED solar EUV experiment, *Phys. Chem. Earth, Part C: Solar, Terr. Planet. Sci.*, *25*(3), 393–396.

Yokota, S., and Y. Saito (2005), Estimation of picked-up lunar ions for future compositional remote SIMS analyses of the lunar surface, *Earth Planets Space*, *57*, 281–289.

Yokota, S., et al. (2009), First direct detection of ions originating from the Moon by MAP-PACE IMA onboard SELENE (KAGUYA), *Geophys. Res. Lett.*, *36*(L11201), doi:10.1029/2009GL038185.